Role of Oxygen States in the Low Valence Nickelate $La_4Ni_3O_8$

Y. Shen,[1,*] J. Sears,[1] G. Fabbris,[2] J. Li,[3] J. Pelliciari,[3] I. Jarrige,[3] Xi He,[1,4] I. Božović,[1,4] M. Mitrano,[5] Junjie Zhang,[6,7] J. F. Mitchell,[6] A. S. Botana,[8] V. Bisogni,[3] M. R. Norman,[6] S. Johnston,[9,10] and M. P. M. Dean[1,†]

[1]*Condensed Matter Physics and Materials Science Department, Brookhaven National Laboratory, Upton, New York 11973, USA*
[2]*Advanced Photon Source, Argonne National Laboratory, Lemont, Illinois 60439, USA*
[3]*National Synchrotron Light Source II, Brookhaven National Laboratory, Upton, New York 11973, USA*
[4]*Department of Chemistry, Yale University, New Haven, Connecticut 06520, USA*
[5]*Department of Physics, Harvard University, Cambridge, Massachusetts 02138, USA*
[6]*Materials Science Division, Argonne National Laboratory, Lemont, Illinois 60439, USA*
[7]*Institute of Crystal Materials, Shandong University, Jinan, Shandong 250100, China*
[8]*Department of Physics, Arizona State University, Tempe, Arizona 85287, USA*
[9]*Department of Physics and Astronomy, The University of Tennessee, Knoxville, Tennessee 37966, USA*
[10]*Institute of Advanced Materials and Manufacturing, The University of Tennessee, Knoxville, Tennessee 37996, USA*

(Received 12 October 2021; revised 13 January 2022; accepted 26 January 2022; published 22 March 2022)

The discovery of superconductivity in square-planar low valence nickelates has ignited a vigorous debate regarding their essential electronic properties: Do these materials have appreciable oxygen charge-transfer character akin to the cuprates, or are they in a distinct Mott-Hubbard regime where oxygen plays a minimal role? Here, we resolve this question using O K-edge resonant inelastic x-ray scattering (RIXS) measurements of the low valence nickelate $La_4Ni_3O_8$ and a prototypical cuprate $La_{2-x}Sr_xCuO_4$ ($x = 0.35$). As expected, the cuprate lies deep in the charge-transfer regime of the Zaanen-Sawatzky-Allen (ZSA) scheme. The nickelate, however, is not well described by either limit of the ZSA scheme and is found to be of mixed charge-transfer–Mott-Hubbard character with the Coulomb repulsion U of similar size to the charge-transfer energy Δ. Nevertheless, the transition-metal-oxygen hopping is larger in $La_4Ni_3O_8$ than in $La_{2-x}Sr_xCuO_4$, leading to a significant superexchange interaction and an appreciable hole occupation of the ligand O orbitals in $La_4Ni_3O_8$ despite its larger Δ. Our results clarify the essential characteristics of low valence nickelates and put strong constraints on theoretical interpretations of superconductivity in these materials.

DOI: 10.1103/PhysRevX.12.011055

Subject Areas: Condensed Matter Physics
Strongly Correlated Materials

I. INTRODUCTION

Creating analogs of the cuprate high-temperature superconductors has been a target of materials research for decades [1–3]. It is widely believed that this requires a formal $d^{9-\delta}$ electron count on the transition-metal (TM) site (as in hole-doped cuprates), strong electronic correlations, and a substantial TM-O hybridization. This situation is illustrated in Fig. 1(a), where the Cu-O charge-transfer energy Δ in cuprates is much smaller than the on-site $3d$ Coulomb repulsion U. Square-planar nickelate materials of the form $R_{n+1}Ni_nO_{2n+2}$ (R stands for a rare earth and n is the number of neighboring NiO_2 layers) realize a $d^{9-\delta}$ valence and were identified as promising potential cuprate analogs [1,4]. This strategy bore fruit when infinite-layer $n = \infty$ $R_{1-x}Sr_xNiO_2$ materials, and more recently, $n = 5$ $Nd_6Ni_5O_{12}$, were shown to superconduct, generating intense scientific interest [5–8].

Even before this discovery, however, it was noted that Ni has a smaller nuclear charge than Cu, which would tend to increase Δ [9]. If Δ is substantially larger, this could potentially realize a Mott-Hubbard situation, as illustrated in Fig. 1(c), in which O states play a minimal role in the low-energy physics. This expectation motivated extensive interest in determining the Mott-Hubbard versus charge-transfer nature of square-planar nickelates, with some researchers categorizing them as Mott-Hubbard systems and others emphasizing the nickelates as cuprate analogs [10–41].

*yshen@bnl.gov
†mdean@bnl.gov

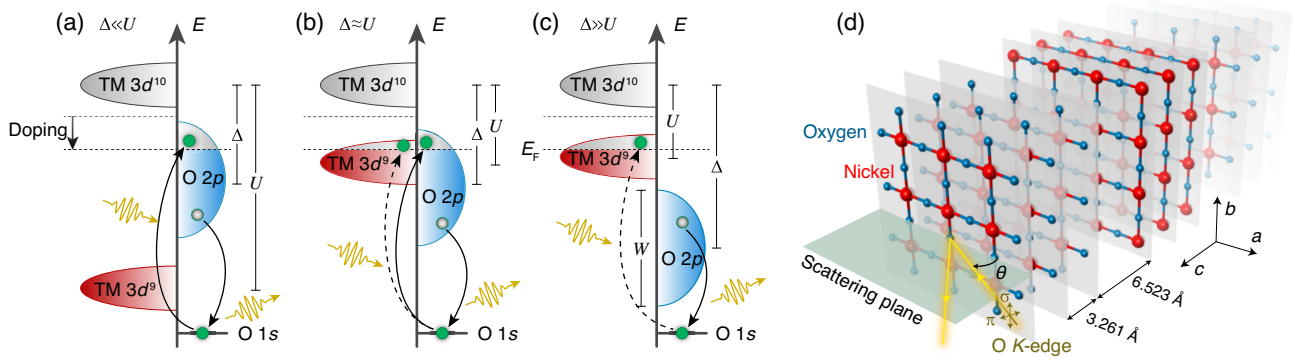

FIG. 1. Schematic of the O K-edge RIXS process. (a)–(c) RIXS processes for different values of the Hubbard U and charge-transfer energy Δ. These are defined as the energy cost of specific atomic transitions in the material: for a d^9 ground state, U being a $d_i^9 d_j^9 \rightarrow d_i^8 d_j^{10}$ and Δ being a $d_i^9 \rightarrow d_i^{10}\underline{L}$ transition, where i and j label TM sites and $\underline{L}$ denotes an oxygen ligand hole. For a charge-transfer insulator ($\Delta \ll U$), the doped holes are mostly in the oxygen $2p$ orbitals, while in a Mott-Hubbard insulator ($\Delta \gg U$), the doped holes mainly occupy the TM $3d^n$ state. In the mixed charge-transfer–Mott-Hubbard regime ($\Delta \sim U$), the doped holes are spread among both the TM and oxygen sites. Arrows show examples of x-ray transition pathways, which, because of x-ray dipole selection rules, can involve either O states or TM-O hybridized states, making this process ideal to distinguish situations (a)–(c). Note that W is the band width for oxygen $2p$ orbitals, and E_F is the Fermi energy (marked by the horizontal dashed lines). (d) Experimental setup for RIXS measurements at the O K edge and crystal structure of $La_4Ni_3O_8$. Only the nickel and oxygen ions in the trilayers are shown.

Resolving this controversy is a crucial step for understanding these materials. The degree of TM-O hybridization is a major determining factor of the relative Ni versus O character of the charge carriers and the magnetic superexchange. This issue also constrains which minimal effective models are appropriate for these materials and is therefore central to understanding nickelate superconductivity. Part of the challenge of this question is that Δ, U, the hopping integrals t_{pd} and t_{pp}, and the crystal field all act together to determine the role of oxygen and the location of the material within the Zaanen-Sawatzky-Allen (ZSA) scheme [42,43]. Progress in this area has also been hindered by varying interpretations based on different experimental approaches [18,36,41,44–48] and the fact that many-body electronic structure results are sensitive to the method used [49]. This controversy has been further amplified by the recent discovery of relatively large superexchange interactions, about half that of cuprates, in both the $n = 3$ and $n = \infty$ materials [44,50]. Resolving these issues requires a spectroscopic probe that can specifically target oxygen states and their energies and an interpretative approach that treats Δ, U, t_{pd}, and t_{pp} on the same footing.

Here, we use O K-edge RIXS to determine the Mott-Hubbard versus charge-transfer electronic characteristics of the $n = 3$ nickelate $La_4Ni_3O_8$, which can be prepared as a bulk single crystal without the need for chemical doping, and the oxygen-containing substrates and capping layers typically required for the stability of the infinite-layer nickelate superconductors. We benchmark our results for this material against a prototypical cuprate $La_{2-x}Sr_xCuO_4$ ($x = 0.35$), which has a similar effective doping. The nickelate is found to be of mixed charge-transfer–Mott-Hubbard electronic character and not well described by either the Zhang-Rice singlet states found in $La_{2-x}Sr_xCuO_4$ nor a Ni-dominated Mott-Hubbard scenario. We confirm this interpretation using exact diagonalization (ED) calculations and further find that the TM-oxygen hopping is enhanced in $La_4Ni_3O_8$ relative to $La_{2-x}Sr_xCuO_4$, with a Δ about 2 eV larger. These parameters lead to a sizable superexchange interaction and an appreciable O character of the doped holes. Our results clarify the essential electronic characteristics of nickelates and imply that both O and Ni are necessary ingredients of minimal effective models for these materials.

II. METHODS

High-energy-resolution RIXS measurements were performed at the SIX beamline at the NSLS-II with an energy resolution of around 22 meV. All data shown were collected at 40 K. We fixed the spectrometer at a horizontal scattering angle $2\Theta = 150°$ and used either π or σ polarized x rays as shown in Fig. 1(d). Thus, we put the crystalline (H, 0, 0) and (0, 0, L) directions in the scattering plane and changed $\boldsymbol{Q}$ by rotating the sample around the vertical (0, 1, 0) axis. Note that θ is defined as the angle between the incident beam and sample surface, which is perpendicular to the sample c axis.

Our chosen low valence nickelate sample is $La_4Ni_3O_8$ [50–54]. This material has a nominal Ni $d^{8\frac{2}{3}}$ valence and can be considered as $1/3$ self-doped with holes. Here, "doped holes" refers to this $\delta = 1/3$ additional holes with respect to d^9, and "holes" refers to the total holes with respect to the closed Ni d shell. With no alkaline earth substitution on the rare-earth site, the $La_4Ni_3O_8$ system presents a well-defined

hole doping and avoids sample inhomogeneity challenges that have hindered studies of $R_{1-x}Sr_xNiO_2$ [36,41,55–58].

Single crystal samples were reduced from the as-grown Ruddlesden-Popper phase $La_4Ni_3O_{10}$ using H_2/Ar gas [51–53] (see the Appendix A for details). $La_4Ni_3O_8$ has a tetragonal structure with space group $I4/mmm$ and lattice constants of $a = b = 3.97$ Å, $c = 26.1$ Å. Its structure features trilayers of square-lattice NiO_2 planes, which are separated by La_2O_2 fluorite blocks [see Fig. 1(d)]. All members of the $R_{n+1}Ni_nO_{2n+2}$ family share very similar Ni-O bonding and would therefore be expected to have similar local correlated physics, provided they are compared at the same effective doping. This expectation is borne out by calculations [25,59] and the similar magnetic exchange [44,50] and superconducting transition temperature in different nickelates [5–8]. We compare $La_4Ni_3O_8$ to $La_{2-x}Sr_xCuO_4$ ($x = 0.35$) samples prepared via molecular beam epitaxy with a similar effective doping as the nickelate.

III. RESULTS AND INTERPRETATION

We start by measuring x-ray absorption spectra of our nickelate and cuprate samples in the O K preedge region, as shown in Figs. 2(a) and 2(c). The spectra have a prepeak feature, which comes from holes occupying TM-O hybridized states [50,52,60,61]. As measured previously, this prepeak is weaker in $La_4Ni_3O_8$ compared to $La_{2-x}Sr_xCuO_4$, but this in itself is insufficient to quantify the electronic nature of these materials in detail [50,52].

Figures 2(b) and 2(d) show the RIXS energy maps at $\theta = 15°$ with σ polarization. The maps consist of strong resonant features that appear at the O K prepeak and diagonal structures of weaker, more diffuse intensity above the resonance. Features that appear as diagonal lines in these maps are assigned to x-ray fluorescence (labeled FL), which occur at constant final energy and arise from a continuum of particle-hole excitations. Apart from the fluorescence line, Raman-like peaks are observed at the prepeak incident energy in both samples, which correspond to local excitations. For $La_4Ni_3O_8$, the resonant signals can be divided into a strong manifold of excitations between 4 and 8 eV (feature A) and a low-energy weaker structure between 1 and 2 eV (feature B) [see Figs. 2(b) and 3(b)]. For $La_{2-x}Sr_xCuO_4$, one manifold of excitations, which we call feature A, covers

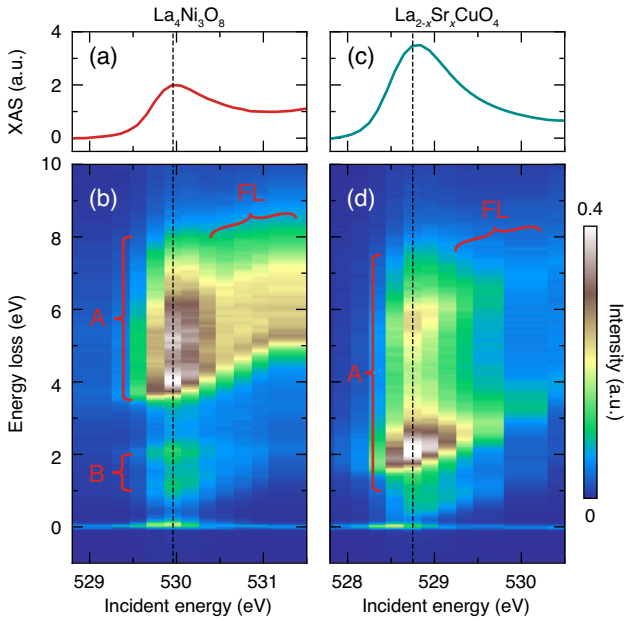

FIG. 2. Comparison of RIXS spectra in $La_4Ni_3O_8$ and $La_{2-x}Sr_xCuO_4$. XAS plots and RIXS intensity maps across the prepeak energies for (a,b) $La_4Ni_3O_8$ and (c,d) $La_{2-x}Sr_xCuO_4$. The data were collected with $\theta = 15°$ and σ polarization. Different contributions can be identified, including the fluorescence (FL) and resonant signals (labeled as features A and B). The vertical dashed lines indicate the prepeak resonant energy. XAS data are shown in arbitrary units (a.u.) normalized to 0 and 1 at energies 1 eV below and 1 eV above the prepeak [50,52].

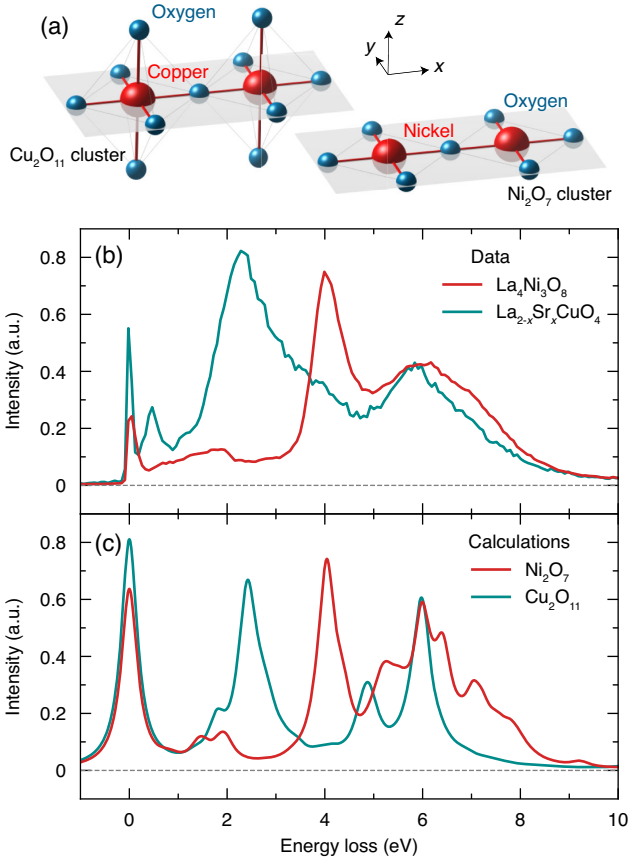

FIG. 3. Cluster exact diagonalization results. (a) Sketch of the clusters used in each case. (b) RIXS curves measured at the O prepeak resonance with $\theta = 60°$ and σ polarization. The feature at 0.5 eV in the $La_{2-x}Sr_xCuO_4$ sample is known to come from a plasmon, so is not expected to appear in our model calculations [62]. (c) Calculated spectra using the parameters listed in Table I with the same experimental geometries.

1–8 eV, making feature B hard to distinguish [see Figs. 2(d) and 3(b)].

In the photon emission process of O K-edge RIXS, electrons from either the TM $3d$ or oxygen $2p$ orbitals can potentially be deexcited to fill the core hole; however, the former channel is expected to be weaker since it is only possible through the TM-O hybridization. In light of this, we might expect feature A to come from charge-transfer excitations in the O $2p$ states and feature B to come from the weaker interorbital dd excitations of the TM $3d$ orbitals. This is further verified by the Ni L-edge RIXS data we have taken, which show a strong peak in the 1–2-eV energy window. The fact that feature A for $La_4Ni_3O_8$ is higher in energy than that in $La_{2-x}Sr_xCuO_4$ indicates a larger Δ by about 2 eV. At the same time, the presence of feature B from dd excitations suggests that there is still appreciable Ni-O hybridization, which would not occur if $\Delta \gg U$. It is also clear that feature A is narrower in the energy loss axis in $La_4Ni_3O_8$, suggesting a smaller oxygen band width, again consistent with the larger Δ. Considering these factors together allows us to conclude that $La_4Ni_3O_8$ is of mixed charge-transfer–Mott-Hubbard character.

To confirm and quantify our conclusion of mixed charge-transfer–Mott-Hubbard character, we make use of cluster ED calculations using the EDRIXS software [63,64] to reveal the electronic structure and oxygen involvement in $La_4Ni_3O_8$ and $La_{2-x}Sr_xCuO_4$. The calculations are performed on Ni_2O_7 and Cu_2O_{11} clusters, respectively, with open boundary conditions and three holes in total (i.e., 1.5 holes per TM site or $x = 0.5$), as shown in Fig. 3(a). The orbital basis in each case includes all five TM $3d$ orbitals and all three O $2p$ orbitals on their respective atoms, and parameters are defined in hole notation such that Δ denotes the energetic splitting between the O and TM states (see Appendixes B and C). More specifically, Δ is defined as the energy cost for a local $d_i^9 \rightarrow d_i^{10}\underline{L}$ transition, and U reflects the energy needed for a $d_i^9 d_j^9 \rightarrow d_i^8 d_j^{10}$ transition [42,43]. Although in undoped d^9 infinite-layer nickelates, the rare-earth orbitals act as effective dopants, dynamical mean field theory (DMFT) calculations suggest that their role is minimal in heavily doped nickelates, where these states are unoccupied and only weakly hybridized with the planar Ni and O orbitals [25]. Omitting rare-earth orbitals allows us to maintain a tractable basis size while still achieving a satisfactory description of the data. Starting from the atomic limit, we explicitly include Coulomb interactions and nearest-neighbor interatomic hopping, and simulate the XAS and RIXS spectra with experimental conditions fully accounted for (see Appendix C for more details). As explained in detail in the Supplemental Material [65], the model parameters were then adjusted to match the experimental spectra, and they are listed in Table I. The strong core-hole potential in RIXS means that the low-energy excitations seen at resonance tend to have rather local character and minimal dispersion, which supports and motivates the widespread cluster-based interpretation of RIXS measurements [67–74].

Our approach fully incorporates many-body and multi-orbital effects, avoiding issues with *ad hoc* parameters or double counting [76,77], and it allows us to directly compare theory and experiment by evaluating the Kramers-Heisenberg equation for the RIXS cross section. In this way, we can extract Δ and U in the original sense defined within the ZSA scheme as outlined in Fig. 1. Other means of extracting these parameters, such as those relying on density functional theory, can potentially be affected by double counting of the Coulomb interactions [65,76,77]. These advantages come at the cost of having to work with a small cluster, which means that the effective doping level ($x = 0.5$) is only approximately that of the real materials ($x \approx 1/3$). Potential minor discrepancies are expected, arising from the small cluster size and omitted interactions with other atoms such as the rare-earth ions and adjacent layers. In addition, the cluster does not capture the FL feature since this requires a continuum of states [41,78]. These factors lead to an error bar of about 1 eV on the extracted parameters, but within this error, the extracted parameters are robust, as has been demonstrated in several prior small cluster calculations of related oxide materials including cuprates and infinite-layer nickelates [67–74].

TABLE I. Representative parameters used for the ED calculations. Full details are provided in Appendix C. Note that U is the on-site intraorbital Coulomb interaction for the $3d$ orbitals, and Δ measures the charge-transfer energy. These parameters have an estimated error bar of about 1 eV [65]. Here, $t_{p_\sigma d_{x^2-y^2}}$ is the hopping integral between planar p_σ and $d_{x^2-y^2}$ orbitals while $t_{p_\sigma p_\sigma}$ is that among the p_σ orbitals. The column labeled J_{calc} is the singlet-triplet energy splitting of the undoped (d^9) cluster (two holes in total), and J_{exp} is the superexchange interaction from experiment. These parameters are given in eV. The column labeled TM holes is the hole occupation of the TM orbitals per TM site of the doped 2-TM site clusters (which have three holes in total). The column labeled O holes is the hole occupation of the oxygen orbitals per TM site.

Cluster	U	Δ	$t_{p_\sigma d_{x^2-y^2}}$	$t_{p_\sigma p_\sigma}$	J_{calc}	J_{exp}	TM holes	O holes
Ni_2O_7	6.5	5.6	1.36	0.375	0.084	0.069 [50]	1.05	0.45
Cu_2O_{11}	9	3.4	1.17	0.625	0.151	0.143 [75]	0.76	0.74

The calculated RIXS spectra are shown in Fig. 3(c) and capture the onset and bandwidth of the spectral features nicely, including feature A, and the fact that feature B is difficult to observe in $La_{2-x}Sr_xCuO_4$. The observed level of agreement is comparable or surpasses the typical level of agreement of theoretical interpretations of O K-edge RIXS spectra [19,70–74].

Table I summarizes the parameters extracted from our theoretical analysis. As expected, these values confirm our empirical conclusions regarding the charge-transfer versus Mott-Hubbard characteristics of $La_4Ni_3O_8$ and $La_{2-x}Sr_xCuO_4$. We find that Δ is much smaller than U in $La_{2-x}Sr_xCuO_4$, confirming its charge-transfer nature, consistent with the known character of cuprates [1–3]. Our $\Delta \sim 3.4$ eV determination is very similar to the literature values from prior ED studies and within 1 eV (slightly larger) of those in first-principles work [74,79]. This is consistent with the estimated 1 eV error bar of our parameter extraction and indicates that the finite-size cluster effect will only change a parameter by less than this error bar. In contrast, $La_4Ni_3O_8$ has a significantly larger $\Delta \sim 5.6$ eV, which is comparable to $U \sim 6.5$ eV. This value places $La_4Ni_3O_8$ in a mixed charge-transfer–Mott-Hubbard regime. It should be noted that different combinations of ED parameters can produce similar RIXS spectra for $La_4Ni_3O_8$, but all of them give a $\Delta \approx 6$ eV within a 1 eV error bar and a U of a similar size to Δ [65]. As a consequence, the nickelate has enhanced Ni hole character compared to the cuprate, but it retains appreciable O hole character and therefore is not in the pure Mott-like regime in which the holes would have overwhelming TM d character. Our fits to the data also find that the $p-d$ hopping is enhanced in $La_4Ni_3O_8$, which we attribute to the more extended nickel d orbitals due to the smaller nuclear charge [80]. Coupled with the fact that Δ is only about 2 eV larger than in the cuprates, this means that a significant portion of the doped holes still reside on the oxygen sites (Table I). At the same time, $La_4Ni_3O_8$ has a larger fraction of $|d^8\rangle$ states in its ground-state wave function compared to $La_{2-x}Sr_xCuO_4$ because of its larger Δ and lower $U \approx \Delta$ (see Appendix D), as also found in DMFT studies [21,25,28]. Overall, the TM-O hybridization, which can be quantified by the parameter t_{pd}^2/Δ, is slightly reduced in $La_4Ni_3O_8$: 0.33 for $La_4Ni_3O_8$ compared to 0.4 for $La_{2-x}Sr_xCuO_4$.

Examining the wave functions in Appendix D, we find that feature A in $La_4Ni_3O_8$ is largely of a charge-transfer type, where a significant fraction of a hole (about 0.43) is excited from the double-hole-occupied Ni ion to the ligand O orbitals (i.e., $|d^8\rangle \rightarrow |d^9\underline{L}\rangle$). In $La_{2-x}Sr_xCuO_4$, the excitation is more mixed; it involves both a small amount of charge transfer (about 0.14 holes) from the Cu to ligand O and a rearrangement of the ligand hole (i.e., $|d^9\underline{L}\rangle \rightarrow |d^9\underline{L}'\rangle$). Feature B, on the other hand, corresponds to dd excitations, where the ground-state occupations of the TM $3d$ orbitals are rearranged during the scattering process. They are also present but weaker in

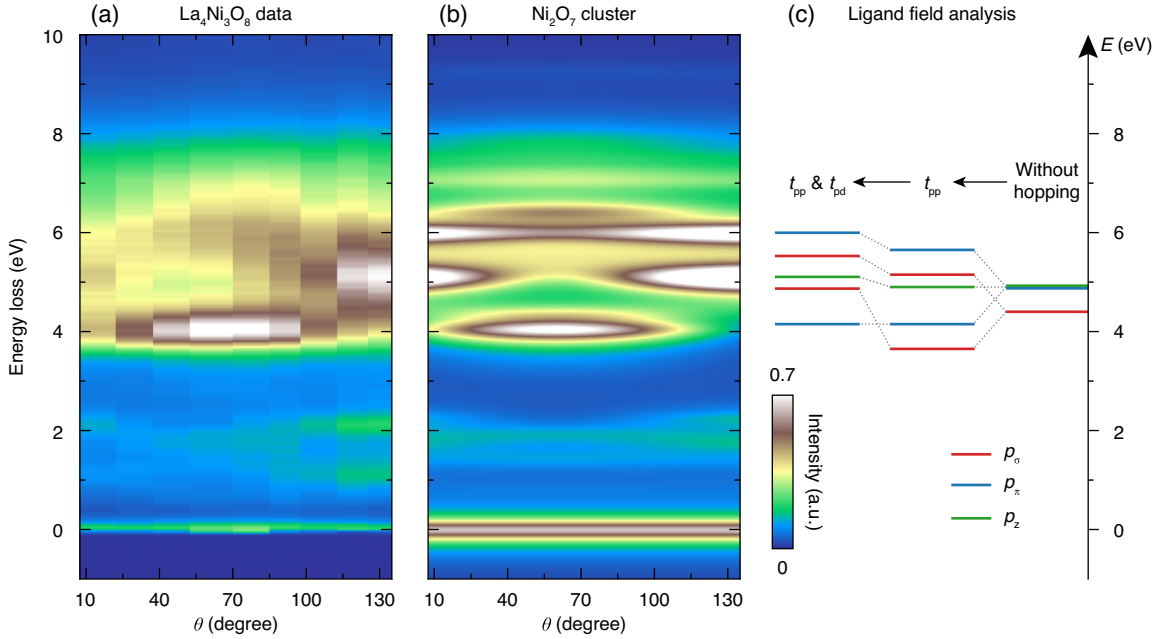

FIG. 4. Angle dependence of $La_4Ni_3O_8$ RIXS intensity at the preedge with σ polarization. (a) RIXS map data after absorption correction. (b) Simulation of a Ni_2O_7 cluster. (c) Orbital energy-level diagram of the multiplet ligand field analysis using the parameters listed in Table I. A full description of these states can be found in Appendix E. Since this breakdown of the different orbitals is based on one-hole basis functions, the y energy axis has been shifted to account for the doping.

the $La_{2-x}Sr_xCuO_4$ calculations and obscured by feature A's overlapping contribution. Detailed projections of the wave functions onto different states are provided in Appendix D.

To further verify our model for $La_4Ni_3O_8$, we show that our ED calculations also capture the angular dependence of the spectra. In this case, the evolution of the RIXS intensity with θ can largely be accounted for by the matrix elements of the RIXS cross section, which select different O orbitals. They can be easily calculated in the dipole approximation, and the results are reasonably consistent with the $La_4Ni_3O_8$ data (Fig. 4). The different levels can be conceptualized using a multiplet ligand field model [82,83], which is a simplified version of the cluster model we use for our full analysis, as explained in Appendix E. In this approach, the O $2p$ orbitals hybridize with each other, forming bonding, antibonding, and nonbonding ligand orbitals through in-plane $p-p$ hopping. Some of these have the same symmetry as the TM $3d$ orbitals and thus hybridize with them via the relevant $p-d$ hopping. Using the parameters determined from our ED calculations, we produce a simplified scheme of the ligand orbital energy levels in Fig. 4(c). Although the ligand orbital splitting is slightly underestimated because of omitted terms in the ligand field analysis—such as the $p_\sigma - p_\pi$ hopping—and multiplet effects are absent in the one-hole basis functions, the overall distribution of the hybridized states is qualitatively consistent with the data and is well captured by our ED calculations.

IV. DISCUSSION

Our detailed RIXS measurements and ED analysis put $La_4Ni_3O_8$ in the mixed charge-transfer–Mott-Hubbard parameter regime of the ZSA scheme. Although the larger Δ in $La_4Ni_3O_8$ suppresses the hybridization of the TM $3d$ and oxygen $2p$ orbitals, the fact that Δ is only about 2 eV larger, along with the enhanced $p-d$ hopping, guarantees that the oxygen orbitals retain a significant role in determining the physical properties of these low valence nickelates. This also results in a substantial superexchange interaction that is half that of the cuprates [50]. In this regard, low valence nickelates are a good analog of cuprate superconductors. However, the larger Δ produces a small, but possibly significant Ni $|d^8\rangle$ weight in the ground state.

Since multiorbital physics has been discussed extensively in nickelates, we compute the involvement of different Ni d orbitals in the ground state. According to our ED calculations, the majority orbital character retains $d_{x^2-y^2}$ symmetry—less than 8% of the holes occupy the $d_{3z^2-r^2}$ orbitals in $La_4Ni_3O_8$ (see Appendix D). Hund's physics therefore has only a small role in determining the properties of this material, and the Ni states are predominantly of low-spin character, consistent with prior experiments [45,50,52]. This is partly due to the strong TM-O hybridization, along with the square-planar environment of Ni, which gives rise to a large crystal field splitting in the e_g states. Since both the $d_{x^2-y^2}$ and $d_{3z^2-r^2}$ orbitals hybridize with the O $2p_\sigma$ orbitals, they can mix despite their different symmetries. If Δ increases further, the $d_{3z^2-r^2}$ orbitals become more involved, as shown in Appendix F.

The mixed charge-transfer–Mott-Hubbard character of the low valence nickelates reported here suggests that minimal theoretical models must explicitly include both Ni and O states alongside strong correlations. In this regime, the properties of many-body methods such as DMFT can become dependent on the choice of basis functions to represent the correlations [49]. Problems with so-called "double counting" of U are also more difficult to avoid in this case [76,77]. Both of these challenges likely contribute to the differences between different studies thus far [10–24,26–41]. By combining O-resonant spectroscopy with an ED treatment of the relevant Δ, U, and hopping parameters, we can confidently report that $La_4Ni_3O_8$ is described by $U \sim \Delta$ with both values of order 6 eV. While our results position $La_4Ni_3O_8$ in the mixed ZSA regime, other factors such as rare-earth orbitals, electron-phonon coupling, and La_2O_2 layers might contribute to the detailed properties of these materials [11,18,59]. However, addressing these more subtle factors would expand the basis size well beyond what can be handled by current state-of-the-art ED calculations and require more approximate means of handling correlations, which is contrary to the goal of providing a rigorous minimal description of these materials.

V. CONCLUSIONS

In summary, we combine RIXS measurements at the O K edge and ED calculations to compare the low valence nickelate $La_4Ni_3O_8$ to a prototypical cuprate $La_{2-x}Sr_xCuO_4$ with a similar nominal electron filling. Our work is unique in directly measuring the energy of the Ni-O hybridized states and interpreting them while treating Δ, U, and hoppings on the same footing. The results reveal that $La_4Ni_3O_8$ has a larger Δ, smaller U, and increased $p-d$ hopping, which gives it a mixed charge-transfer–Mott-Hubbard electronic character. Despite its larger Δ, the nickelate retains a sizable superexchange through its strong hopping. Moreover, for the parameters we have determined, Hund's physics is less relevant than might be expected (i.e., despite the admixture of d^8), consistent with the square-planar environment of Ni. Given that $La_4Ni_3O_8$ and $NdNiO_2$ have similar magnetic exchange interactions [44,50], and since magnetic exchange is very sensitive to the Δ/U ratio, we suggest that this mixed charge-transfer–Mott-Hubbard picture likely applies to the entire $R_{n+1}Ni_nO_{2n+2}$ series. This idea

is also supported by first-principles calculations, which find that these materials are indeed rather similar, provided they are compared at the same effective doping [25,59]. Overall, we conclude that both the Coulomb interactions and charge-transfer processes need to be considered when interpreting the properties of these nickelates. Realistic models of low valence nickelates must therefore include both Ni and O states at a minimum, and we suggest this as a basis for conceptualizing these fascinating materials.

The supporting data for the plots in this article are openly available from the Zenodo database [84].

ACKNOWLEDGMENTS

We thank Kenji Ishii for helpful discussions. Work at Brookhaven National Laboratory (RIXS measurement and interpretation, and cuprate sample synthesis) was supported by the U.S. Department of Energy (DOE), Office of Science, Office of Basic Energy Sciences. Work at Argonne was supported by the U.S. DOE, Office of Science, Basic Energy Sciences, Materials Science and Engineering Division (nickelate sample synthesis and first-principles calculations). A. B. acknowledges support from NSF Grant No. DMR 2045826. S. J. acknowledges support from the U.S. DOE, Office of Science, Office of Basic Energy Sciences, under Award No. DE-SC0022311. X. H. was supported by the Gordon and Betty Moore Foundation's EPiQS Initiative through Grant No. GBMF9074. This research used resources at the SIX beamline of the National Synchrotron Light Source II, a U.S. DOE Office of Science User Facility operated for the DOE Office of Science by Brookhaven National Laboratory under Contract No. DE-SC0012704. This research used resources of the Advanced Photon Source, a U.S. DOE Office of Science User Facility at Argonne National Laboratory, and is based on research supported by the U.S. DOE Office of Science-Basic Energy Sciences, under Contract No. DE-AC02-06CH11357.

APPENDIX A: SAMPLE SYNTHESIS AND CHARACTERIZATION

The $La_4Ni_3O_8$ single crystal used in this study was prepared as described in Refs. [51,52] and was the same piece as was used in Ref. [50]. The parent Ruddlesden-Popper $La_4Ni_3O_{10}$ was prepared using the high-pressure optical floating zone method. During growth, oxygen gas was maintained at 20-bar pressure with a flow rate of 0.1 l/min. To improve homogeneity, the feed and seed rods were counterrotated at 30 rpm, and rods were advanced at 4 mm/h over the 30-hour growth time. Sample reduction was performed by heating small crystals cleaved from the parent $La_4Ni_3O_{10}$ boule in a flowing 4% H_2/Ar gas mixture at 350 °C for five days.

The $La_{2-x}Sr_xCuO_4$ film reported here was synthesized using the atomic-layer-by-layer molecular beam epitaxy (ALL-MBE) technique [85], in a similar way to samples used for prior RIXS studies [86–88]. Our ALL-MBE system contains 16 metal sources (thermal-effusion or Knudsen cells) and a source of pure (distilled) ozone. The growth is monitored in real time by means of reflection high-energy electron diffraction (RHEED), which provides information about the time evolution of the film surface morphology and crystal structure [89]. The growth kinetics is controlled using pneumatic linear-motion actuators that shutter the atomic sources. The $La_{2-x}Sr_xCuO_4$ film studied here is heavily overdoped, $x = 0.35$. It was grown on a 10×10-mm^2 single-crystal $LaSrAlO_4$ substrate polished with the [001] axis perpendicular to the surface, with a miscut of less than 0.10°. The $LaSrAlO_4$ substrate lattice constants are $a_0 = b_0 = 3.755$ Å, $c_0 = 12.56$ Å. The $La_{2-x}Sr_xCuO_4$ film is 40 unit cells (530 Å) thick, and it is pseudomorphic with the $LaSrAlO_4$ substrate; thus, it is under a small 0.5% compressive strain [90]. Since $LaSrAlO_4$ has no prepeak, it does not contribute to the measured signal. The substrate temperature during the growth (measured by a two-color pyrometer) was kept at $T = 611$°C, and the ozone partial pressure was fixed at $p = 3 \times 10^{-5}$ Torr. The growth rate was about 0.03 Å/ sec. After the deposition, the film was annealed for 3.5 hours at $T = 611$°C in an ozone partial pressure $p = 1 \times 10^{-4}$ Torr, and then cooled down slowly at the same pressure.

APPENDIX B: NOTATION OF TRANSITION-METAL AND OXYGEN ORBITALS

For isolated atoms, the TM $3d$ and oxygen $2p$ orbitals are fully localized. In a compound, however, the hybridization among atoms will mix these orbitals, and the wave functions of the eigenstate orbitals are composed of different atomic-character Wannier orbitals.

In the clusters used in this study, shown in Fig. 3(a) of the main text, the TM sites are all equivalent and include $d_{x^2-y^2}$, $d_{3z^2-r^2}$, d_{xy}, and $d_{xz/yz}$ orbitals. Oxygen atoms include p_x, p_y, p_z orbitals, and they exist in inequivalent planar and apical locations; thus, we use p and p^a to distinguish them. The planar oxygen orbitals can be represented using p_σ and p_π orbitals that are parallel and perpendicular to the TM-O bonds, respectively, and that are composed of different p_x, p_y, and p_z orbitals depending on the site. To further distinguish between the in-plane and out-of-plane p_π-type orbitals, we refer to the in-plane ones as p_π and the out-of-plane ones as just p_z. For the apical oxygens, two sets of p^a_π orbitals are equivalent, and p^a_σ orbitals are labeled simply as p^a_z.

TABLE II. Full list of parameters used for the ED calculations, including the full set of TM $3d$ and oxygen $2p$ orbital energies. We set $\epsilon_{d_{x^2-y^2}} = 0$, which means that, within hole notation, we need to set $\epsilon_{p_\sigma} = \Delta$ [65]. Note that $V_{pd\sigma}$, $V_{pd\pi}$, $V_{pp\sigma}$, and $V_{pp\pi}$ are amplitudes of Slater-Koster parameters, and we fix $V_{pd\pi} = -V_{pd\sigma}/2$ and $V_{pp\pi} = -V_{pp\sigma}/4$. Correspondingly, $t_{p_\sigma p_\sigma} = (V_{pp\sigma} - V_{pp\pi})/2$ and $t_{p_\sigma d_{x^2-y^2}} = \sqrt{3}V_{pd\sigma}/2$. Here, η is the ratio of the out-of-plane TM-O distance over the in-plane one, which controls the hopping amplitudes involving the apical oxygen. We assume $V_{pp\sigma}$ scales with d^{-2}, where d is the O-O bond length, and $V_{pd\sigma}$ scales with $d^{-3.5}$, where d is the TM-O bond length [82]. Here, F^0_{dd}, F^2_{dd}, and F^4_{dd} are Slater integrals for the TM $3d$ orbitals, and F^0_{pp} and F^2_{pp} are for oxygen $2p$. Correspondingly, $U = F^0_{dd} + 4/49 \times (F^2_{dd} + F^4_{dd})$, and the Hund's coupling is $J_H = (F^2_{dd} + F^4_{dd})/14$. Note that U_{dp} is the intersite Coulomb interaction between TM $3d$ and oxygen $2p$ holes, and U_q is the core-hole potential for oxygen. Here, Δ and U have an estimated error bar of about 1 eV [65]. All parameters, with the exception of η, are in units of eV.

Cluster	$\epsilon_{d_{x^2-y^2}}$	$\epsilon_{d_{3z^2-r^2}}$	$\epsilon_{d_{xy}}$	$\epsilon_{d_{xz/yz}}$	ϵ_{p_σ}	ϵ_{p_π/p_z}	$\epsilon_{p^a_\pi}$	$\epsilon_{p^a_z}$	$V_{pd\sigma}$	$V_{pp\sigma}$	η	F^0_{dd}	F^2_{dd}	F^4_{dd}	F^0_{pp}	F^2_{pp}	U_{dp}	U_q
Cu_2O_{11}	0	0.95	0.7	0.9	3.4	4	4	3.4	1.35	1	1.3	7.86	8.61	5.38	3.3	5	1	6
Ni_2O_7	0	0.2	0.1	0.3	5.6	6.1	⋯	⋯	1.57	0.6	⋯	5.58	6.89	4.31	3.3	5	1	6

APPENDIX C: CLUSTER EXACT DIAGONALIZATION CALCULATIONS

For this work, we compute the RIXS cross section using the cluster ED approach. This accurately treats interactions and cross-section effects and is widely used to treat localized direct RIXS processes in correlated oxides [67–74,91]. This makes it appropriate for simulating features A and B, although it fails to capture x-ray fluorescence. The full Hamiltonian is composed of several terms:

$$\mathcal{H} = \hat{E}_d + \hat{E}_p + \hat{\Delta} + \hat{U}_{dd} + \hat{U}_{pp} + \hat{U}_{dp} + \hat{U}_q + \hat{T}_{pp} + \hat{T}_{dp}, \tag{C1}$$

where $\hat{E}_d$ and $\hat{E}_p$ are the on-site energies of TM $3d$ and oxygen $2p$ orbitals, respectively, and $\hat{\Delta}$ is the charge-transfer energy. The point-charge crystal electric field (CEF) splitting is included in these terms. Here, $\hat{U}_{dd}$ and $\hat{U}_{pp}$ describe the on-site Coulomb interactions for the TM and oxygen, respectively. All the Coulomb and exchange integrals are included explicitly. Note that $\hat{U}_{dp}$ is the intersite Coulomb interaction between TM and oxygen. For the intermediate states, an additional term, $\hat{U}_q$, is included to account for the core-hole potential. Here, $\hat{T}_{pp}$ and $\hat{T}_{dp}$ refer to O-O $p-p$ hopping and TM-O $p-d$ hopping, respectively. All the hopping integrals are evaluated from the Slater-Koster parameters. The hopping terms involving apical oxygen are renormalized according to the bond lengths for the Cu_2O_{11} cluster [82]. The hopping phases are explicitly considered in the Hamiltonian. For simplicity spin-orbit coupling is not considered. The full set of parameters used for calculating the spectra presented in the main text are listed in Table II.

Regarding the Hilbert space, we include all the spin-resolved TM $3d$ and oxygen $2p$ orbitals and perform ED in the two-up, one-down spin sector for the doped clusters (three holes). For the undoped clusters (two holes), all the spin configurations are included. The Hamiltonian is constructed in the hole language. In this case, Δ is the energy difference between the $d_{x^2-y^2}$ and p_σ orbitals regardless of the Coulomb interactions. In addition, by definition, U equals the intraorbital on-site Coulomb interaction for a d^9 system [42,43]. The resulting eigenstates for the initial, intermediate, and final states from ED are used to calculate the XAS and RIXS spectra using the Kramers-Heisenberg formula in the dipole approximation with the experimental geometry explicitly considered. The inverse core-hole lifetime is fixed to 0.25 eV according to XAS data, and the final-state energy loss spectra are broadened using a Lorentzian function with $\sigma = 0.2$ to account for the band width that is not captured by the small cluster. We sum up the spectra from clusters rotated by 90° around the z axis to restore the C_4 symmetry. These calculations are compared with the experimental intensity after a simple self-absorption correction has been applied to the data based on the incident and emitted x-ray angles with respect to the surface [92].

APPENDIX D: WAVE-FUNCTION ANALYSIS OF ED CALCULATIONS

To reveal the nature of the RIXS spectral features, we show in Fig. 5 the weights of different configurations of the excited states as well as the hole occupations. As discussed in the main text, feature A in $La_{2-x}Sr_xCuO_4$ is dominated by the rearrangement of ligand orbitals, while for $La_4Ni_3O_8$, it involves a significant portion of charge transfer from Ni to O. In another aspect, feature B, which is mostly dd excitations, is clearly identified in $La_4Ni_3O_8$ since it is well separated from feature A. In $La_{2-x}Sr_xCuO_4$, it is weak and obscured by feature A.

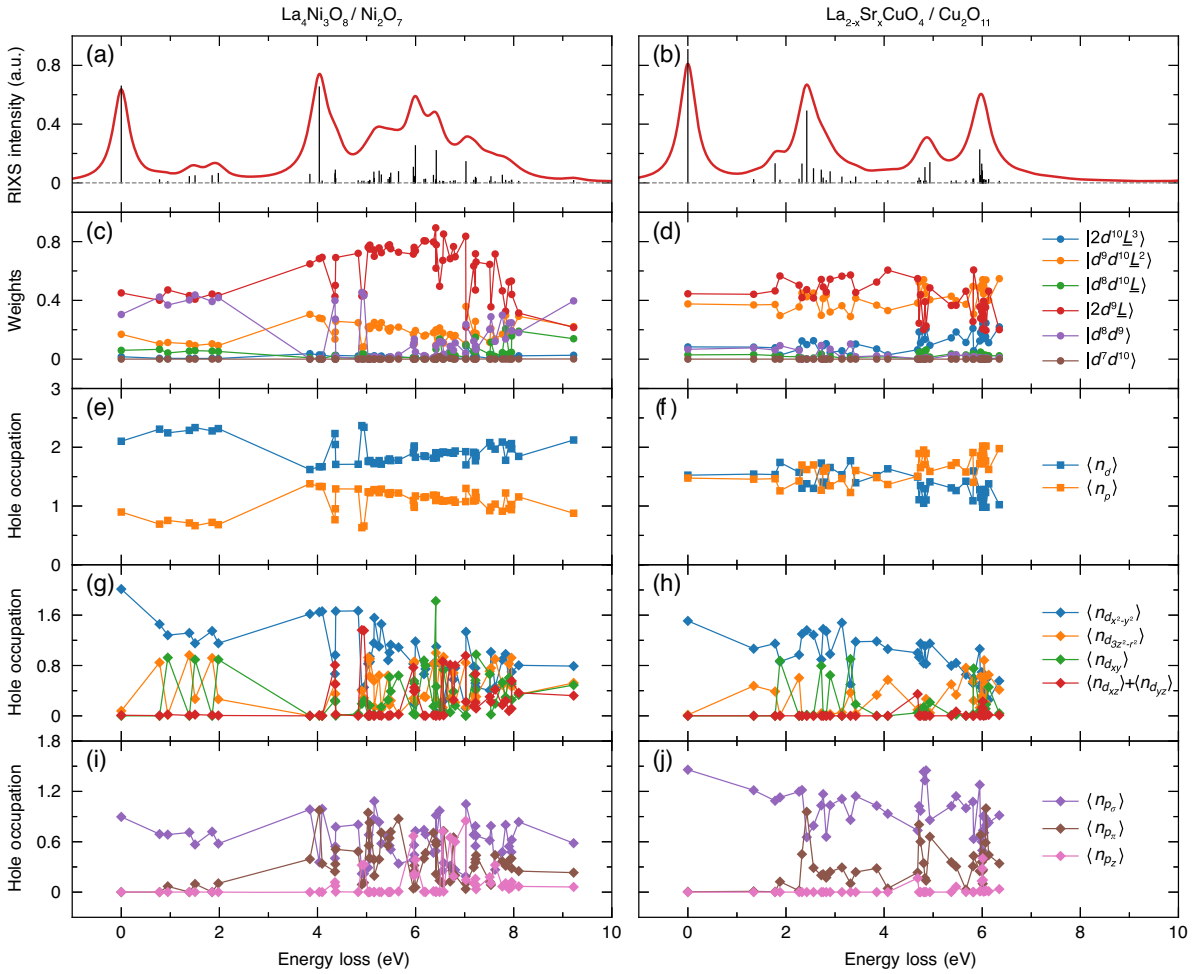

FIG. 5. Wave-function analysis of Ni_2O_7 and Cu_2O_{11} clusters with three holes. (a,b) Calculated unbroadened RIXS intensity (black vertical lines) and broadened RIXS spectra (red curves) with $\theta = 60°$ and σ polarization. Note that in this geometry, the contribution from p_z orbitals is minimized. (c,d) Weights of different configurations of the ground and excited states. (e,f) Hole occupations of TM $3d$ and O $2p$ orbitals. (g,h) Hole occupations for each type of $3d$ orbital. (i,j) Hole occupations for each type of $2p$ orbital. Only the excited states with unbroadened RIXS intensity stronger than 1% of the maximum value are shown.

APPENDIX E: MULTIPLET LIGAND FIELD ANALYSIS

Here, we provide a qualitative explanation of the multiplet ligand field analysis in Fig. 4(c). The analysis is the same as that derived more formally in Ref. [82]. For simplicity, we consider the hybridization of one hole in a NiO_4 cluster. When comparing to $La_4Ni_3O_8$, the sample's doping level is accounted for by offsetting the energy of these states when plotting the different hybridized orbital energies in Fig. 4(c). We start by considering the orbitals in the absence of $p_\sigma - p_\pi$ hopping, such that the four p_σ orbitals in a NiO_4 plaquette will hybridize with each other to form bonding and antibonding molecular orbitals. The nonbonding orbitals are not included [68,82]. The same thing happens for p_π orbitals, while p_z orbitals remain nonbonding if the weak $p_z - p_z$ hopping is ignored. The bonding p_σ molecular orbital has the same symmetry as the nickel $d_{3z^2-r^2}$ orbital, so they will hybridize with each other through $p_\sigma - d_{3z^2-r^2}$ hopping. The same applies for antibonding p_σ molecular and $d_{x^2-y^2}$ orbitals, bonding p_π and d_{xy} orbitals, and the nonbonding p_z and $d_{xz/yz}$ orbitals. The energy levels and hopping integrals are listed in Table III. Note that the antibonding p_π orbital will not hybridize with nickel d due to phase cancellation.

TABLE III. Energy-level splitting of the one-hole basis functions. The O p orbitals (on-site energies ϵ_{p_σ}, ϵ_{p_π}, ϵ_{p_z}) hybridize with each other to form ligand orbitals (energies ϵ_L), which further hybridize with TM d orbitals (energies ϵ_d). Here, V are the hopping integrals, and $T_{pp} = V_{pp\sigma} - V_{pp\pi}$. Note that the antibonding molecular p_π ligand orbital that has an energy of $\epsilon_{p_\pi} - T_{pp}$ (not listed) will not hybridize with the TM d states.

Symmetry	ϵ_d	ϵ_L	V
$x^2 - y^2$	$\epsilon_{d_{x^2-y^2}}$	$\epsilon_{p_\sigma} - T_{pp}$	$\sqrt{3}\lvert V_{pd\sigma}\rvert$
$3z^2 - r^2$	$\epsilon_{d_{3z^2-r^2}}$	$\epsilon_{p_\sigma} + T_{pp}$	$\lvert V_{pd\sigma}\rvert$
xy	$\epsilon_{d_{xy}}$	$\epsilon_{p_\pi} + T_{pp}$	$2\lvert V_{pd\pi}\rvert$
xz/yz	$\epsilon_{d_{xz/yz}}$	ϵ_{p_z}	$\sqrt{2}\lvert V_{pd\pi}\rvert$

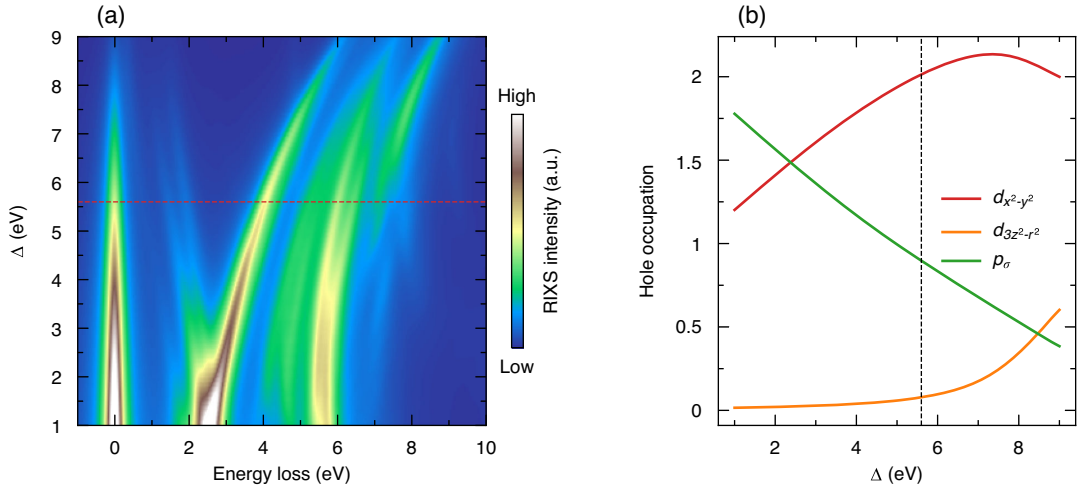

FIG. 6. Ni_2O_7 cluster calculations with different Δ. Other parameters are fixed according to Table II. (a) Intensity map presenting the calculated Δ-dependent RIXS spectra with $\theta = 60°$ and σ polarization. (b) Orbital occupation of holes with different Δ in a doped cluster (three holes) with $U = 6.5$ eV.

APPENDIX F: Δ DEPENDENCE OF RIXS SPECTRA AND HOLE OCCUPATION

Here, we present additional Ni_2O_7 cluster ED results to show how RIXS spectra and hole occupations evolve with Δ. When Δ is small, only feature A can be resolved with an onset below 2 eV, resembling the cuprate data [see Fig. 6(a)]. Concomitantly, the holes mainly occupy the oxygen sites [see Fig. 6(b)]. With increasing Δ, feature A shifts to higher energy, and feature B starts to emerge out of feature A. This also increases the number of holes transferred to the nickel sites. The red and black dashed lines indicate the Δ for $La_4Ni_3O_8$ where feature A and feature B are well separated, but a significant portion of the holes remain on the oxygen sites. As Δ increases further, the $d_{x^2-y^2}$ hole concentration first increases, and then the $d_{3z^2-r^2}$ orbitals come into play, leading to multiorbital physics.

[1] V. Anisimov, D. Bukhvalov, and T. Rice, *Electronic Structure of Possible Nickelate Analogs to the Cuprates*, Phys. Rev. B **59**, 7901 (1999).

[2] M. R. Norman, *Materials Design for New Superconductors*, Rep. Prog. Phys. **79**, 074502 (2016).

[3] R. Adler, C.-J. Kang, C.-H. Yee, and G. Kotliar, *Correlated Materials Design: Prospects and Challenges*, Rep. Prog. Phys. **82**, 012504 (2019).

[4] V. V. Poltavets, K. A. Lokshin, A. H. Nevidomskyy, M. Croft, T. A. Tyson, J. Hadermann, G. Van Tendeloo, T. Egami, G. Kotliar, N. ApRoberts-Warren, A. P. Dioguardi, N. J. Curro, and M. Greenblatt, *Bulk Magnetic Order in a Two-Dimensional* Ni^{1+}/Ni^{2+} (d^9/d^8) *Nickelate, Isoelectronic with Superconducting Cuprates*, Phys. Rev. Lett. **104**, 206403 (2010).

[5] D. Li, K. Lee, B. Y. Wang, M. Osada, S. Crossley, H. R. Lee, Y. Cui, Y. Hikita, and H. Y. Hwang, *Superconductivity in an Infinite-Layer Nickelate*, Nature (London) **572**, 624 (2019).

[6] M. Osada, B. Y. Wang, B. H. Goodge, K. Lee, H. Yoon, K. Sakuma, D. Li, M. Miura, L. F. Kourkoutis, and H. Y. Hwang, *A Superconducting Praseodymium Nickelate with Infinite Layer Structure*, Nano Lett. **20**, 5735 (2020).

[7] S. W. Zeng, C. J. Li, L. E. Chow, Y. Cao, Z. T. Zhang, C. S. Tang, X. M. Yin, Z. S. Lim, J. X. Hu, P. Yang, and A. Ariando, *Superconductivity in Infinite-Layer Lanthanide Nickelates*, arXiv:2105.13492.

[8] G. A. Pan, D. F. Segedin, H. LaBollita, Q. Song, E. M. Nica, B. H. Goodge, A. T. Pierce, S. Doyle, S. Novakov, D. C. Carrizales *et al.*, *Superconductivity in a Quintuple-Layer Square-Planar Nickelate*, Nat. Mater. **21**, 160 (2022).

[9] K.-W. Lee and W. E. Pickett, *Infinite-Layer* $LaNiO_2$*:* Ni^{1+} *Is Not* Cu^{2+}, Phys. Rev. B **70**, 165109 (2004).

[10] L.-H. Hu and C. Wu, *Two-Band Model for Magnetism and Superconductivity in Nickelates*, Phys. Rev. Research **1**, 032046(R) (2019).

[11] Y. Nomura, M. Hirayama, T. Tadano, Y. Yoshimoto, K. Nakamura, and R. Arita, *Formation of a Two-Dimensional Single-Component Correlated Electron System and Band Engineering in the Nickelate Superconductor* $NdNiO_2$, Phys. Rev. B **100**, 205138 (2019).

[12] H. Sakakibara, H. Usui, K. Suzuki, T. Kotani, H. Aoki, and K. Kuroki, *Model Construction and a Possibility of Cupratelike Pairing in a New* d^9 *Nickelate Superconductor* $(Nd,Sr)NiO_2$, Phys. Rev. Lett. **125**, 077003 (2020).

[13] G. A. Sawatzky, *Superconductivity Seen in a Non-magnetic Nickel Oxide*, Nature (London) **572**, 592 (2019).

[14] P. Adhikary, S. Bandyopadhyay, T. Das, I. Dasgupta, and T. Saha-Dasgupta, *Orbital-Selective Superconductivity in a Two-Band Model of Infinite-Layer Nickelates*, Phys. Rev. B **102**, 100501(R) (2020).

[15] B.-X. Wang, H. Zheng, E. Krivyakina, O. Chmaissem, P. P. Lopes, J. W. Lynn, L. C. Gallington, Y. Ren, S. Rosenkranz,

J. Mitchell *et al.*, *Synthesis and Characterization of Bulk* $Nd_{1-x}Sr_xNiO_2$ *and* $Nd_{1-x}Sr_xNiO_3$, Phys. Rev. Mater. **4**, 084409 (2020).

[16] A. S. Botana and M. R. Norman, *Similarities and Differences between* $LaNiO_2$ *and* $CaCuO_2$ *and Implications for Superconductivity*, Phys. Rev. X **10**, 011024 (2020).

[17] M.-Y. Choi, W. E. Pickett, and K.-W. Lee, *Fluctuation-Frustrated Flat Band Instabilities in* $NdNiO_2$, Phys. Rev. Research **2**, 033445 (2020).

[18] M. Hepting, D. Li, C. Jia, H. Lu, E. Paris, Y. Tseng, X. Feng, M. Osada, E. Been, Y. Hikita *et al.*, *Electronic Structure of the Parent Compound of Superconducting Infinite-Layer Nickelates*, Nat. Mater. **19**, 381 (2020).

[19] M. Jiang, M. Berciu, and G. A. Sawatzky, *Critical Nature of the Ni Spin State in Doped* $NdNiO_2$, Phys. Rev. Lett. **124**, 207004 (2020).

[20] F. Lechermann, *Late Transition Metal Oxides with Infinite-Layer Structure: Nickelates versus Cuprates*, Phys. Rev. B **101**, 081110(R) (2020).

[21] F. Lechermann, *Doping-Dependent Character and Possible Magnetic Ordering of* $NdNiO_2$, Phys. Rev. Mater. **5**, 044803 (2021).

[22] Z. Liu, Z. Ren, W. Zhu, Z. Wang, and J. Yang, *Electronic and Magnetic Structure of Infinite-Layer* $NdNiO_2$*: Trace of Antiferromagnetic Metal*, npj Quantum Mater. **5**, 31 (2020).

[23] F. Petocchi, V. Christiansson, F. Nilsson, F. Aryasetiawan, and P. Werner, *Normal State of* $Nd_{1-x}Sr_xNiO_2$ *from Self-Consistent* $GW + \mathrm{EDMFT}$, Phys. Rev. X **10**, 041047 (2020).

[24] J. Karp, A. S. Botana, M. R. Norman, H. Park, M. Zingl, and A. Millis, *Many-Body Electronic Structure of* $NdNiO_2$ *and* $CaCuO_2$, Phys. Rev. X **10**, 021061 (2020).

[25] J. Karp, A. Hampel, M. Zingl, A. S. Botana, H. Park, M. R. Norman, and A. J. Millis, *Comparative Many-Body Study of* $Pr_4Ni_3O_8$ *and* $NdNiO_2$, Phys. Rev. B **102**, 245130 (2020).

[26] J. Kapeghian and A. S. Botana, *Electronic Structure and Magnetism in Infinite-Layer Nickelates* $RNiO_2$ $(R = \mathrm{La} - \mathrm{Lu})$, Phys. Rev. B **102**, 205130 (2020).

[27] Y. Nomura, T. Nomoto, M. Hirayama, and R. Arita, *Magnetic Exchange Coupling in Cuprate-Analog* d^9 *Nickelates*, Phys. Rev. Research **2**, 043144 (2020).

[28] Y. Wang, C.-J. Kang, H. Miao, and G. Kotliar, *Hund's Metal Physics: From* $SrNiO_2$ *to* $LaNiO_2$, Phys. Rev. B **102**, 161118(R) (2020).

[29] P. Werner and S. Hoshino, *Nickelate Superconductors: Multiorbital Nature and Spin Freezing*, Phys. Rev. B **101**, 041104(R) (2020).

[30] X. Wu, D. Di Sante, T. Schwemmer, W. Hanke, H. Y. Hwang, S. Raghu, and R. Thomale, *Robust* $d_{x^2-y^2}$*-Wave Superconductivity of Infinite-Layer Nickelates*, Phys. Rev. B **101**, 060504(R) (2020).

[31] H. Zhang, L. Jin, S. Wang, B. Xi, X. Shi, F. Ye, and J.-W. Mei, *Effective Hamiltonian for Nickelate Oxides* $Nd_{1-x}Sr_xNiO_2$, Phys. Rev. Research **2**, 013214 (2020).

[32] G.-M. Zhang, Y.-f. Yang, and F.-C. Zhang, *Self-Doped Mott Insulator for Parent Compounds of Nickelate Superconductors*, Phys. Rev. B **101**, 020501(R) (2020).

[33] Y.-H. Zhang and A. Vishwanath, *Type-II* $t - J$ *Model in Superconducting Nickelate* $Nd_{1-x}Sr_xNiO_2$, Phys. Rev. Research **2**, 023112 (2020).

[34] S. Zeng, C. S. Tang, X. Yin, C. Li, M. Li, Z. Huang, J. Hu, W. Liu, G. J. Omar, H. Jani, Z. S. Lim, K. Han, D. Wan, P. Yang, S. J. Pennycook, A. T. S. Wee, and A. Ariando, *Phase Diagram and Superconducting Dome of Infinite-Layer* $Nd_{1-x}Sr_xNiO_2$ *Thin Films*, Phys. Rev. Lett. **125**, 147003 (2020).

[35] E. Been, W.-S. Lee, H. Y. Hwang, Y. Cui, J. Zaanen, T. Devereaux, B. Moritz, and C. Jia, *Electronic Structure Trends across the Rare-Earth Series in Superconducting Infinite-Layer Nickelates*, Phys. Rev. X **11**, 011050 (2021).

[36] B. H. Goodge, D. Li, K. Lee, M. Osada, B. Y. Wang, G. A. Sawatzky, H. Y. Hwang, and L. F. Kourkoutis, *Doping Evolution of the Mott–Hubbard Landscape in Infinite-Layer Nickelates*, Proc. Natl. Acad. Sci. U.S.A. **118**, e2007683118 (2021).

[37] Z.-J. Lang, R. Jiang, and W. Ku, *Strongly Correlated Doped Hole Carriers in the Superconducting Nickelates: Their Location, Local Many-Body State, and Low-Energy Effective Hamiltonian*, Phys. Rev. B **103**, L180502 (2021).

[38] C.-J. Kang and G. Kotliar, *Optical Properties of the Infinite-Layer* $La_{1-x}Sr_xNiO_2$ *and Hidden Hund's Physics*, Phys. Rev. Lett. **126**, 127401 (2021).

[39] T. Plienbumrung, M. Daghofer, and A. M. Ole, *Interplay between Zhang-Rice Singlets and High-Spin States in a Model for Doped* NiO_2 *Planes*, Phys. Rev. B **103**, 104513 (2021).

[40] X. Wan, V. Ivanov, G. Resta, I. Leonov, and S. Y. Savrasov, *Exchange Interactions and Sensitivity of the Ni Two-Hole Spin State to Hund's Coupling in Doped* $NdNiO_2$, Phys. Rev. B **103**, 075123 (2021).

[41] K. Higashi, M. Winder, J. Kune, and A. Hariki, *Core-Level X-Ray Spectroscopy of Infinite-Layer Nickelate:* $\mathrm{LDA} + \mathrm{DMFT}$ *Study*, Phys. Rev. X **11**, 041009 (2021).

[42] J. Zaanen, G. A. Sawatzky, and J. W. Allen, *Band Gaps and Electronic Structure of Transition-Metal Compounds*, Phys. Rev. Lett. **55**, 418 (1985).

[43] J. Zaanen and G. A. Sawatzky, *The Electronic Structure and Superexchange Interactions in Transition-Metal Compounds*, Can. J. Phys. **65**, 1262 (1987).

[44] H. Lu, M. Rossi, A. Nag, M. Osada, D. F. Li, K. Lee, B. Y. Wang, M. Garcia-Fernandez, S. Agrestini, Z. X. Shen, E. M. Been, B. Moritz, T. P. Devereaux, J. Zaanen, H. Y. Hwang, K.-J. Zhou, and W. S. Lee, *Magnetic Excitations in Infinite-Layer Nickelates*, Science **373**, 213 (2021).

[45] M. Rossi, H. Lu, A. Nag, D. Li, M. Osada, K. Lee, B. Y. Wang, S. Agrestini, M. Garcia-Fernandez, J. J. Kas, Y.-D. Chuang, Z. X. Shen, H. Y. Hwang, B. Moritz, K.-J. Zhou, T. P. Devereaux, and W. S. Lee, *Orbital and Spin Character of Doped Carriers in Infinite-Layer Nickelates*, Phys. Rev. B **104**, L220505 (2021).

[46] Y. Fu, L. Wang, H. Cheng, S. Pei, X. Zhou, J. Chen, S. Wang, R. Zhao, W. Jiang, C. Liu *et al.*, *Core-Level X-Ray Photoemission and Raman Spectroscopy Studies on Electronic Structures in Mott-Hubbard Type Nickelate Oxide* $NdNiO_2$, arXiv:1911.03177.

[47] Q. Gu, Y. Li, S. Wan, H. Li, W. Guo, H. Yang, Q. Li, X. Zhu, X. Pan, Y. Nie, and H.-H. Wen, *Single Particle Tunneling Spectrum of Superconducting* $Nd_{1-x}Sr_xNiO_2$ *Thin Films*, Nat. Commun. **11**, 6027 (2020).

[48] Z. Chen, M. Osada, D. Li, E. M. Been, S.-D. Chen, M. Hashimoto, D. Lu, S.-K. Mo, K. Lee, B. Y. Wang, F. Rodolakis, J. L. McChesney, C. Jia, B. Moritz, T. P. Devereaux, H. Y. Hwang, and Z.-X. Shen, *Electronic Structure of Superconducting Nickelates Probed by Resonant Photoemission Spectroscopy*, arXiv:2106.03963.

[49] J. Karp, A. Hampel, and A. J. Millis, *Dependence of* DFT + DMFT *Results on the Construction of the Correlated Orbitals*, Phys. Rev. B **103**, 195101 (2021).

[50] J. Q. Lin *et al.*, *Strong Superexchange in a* $d^{9-\delta}$ *Nickelate Revealed by Resonant Inelastic X-Ray Scattering*, Phys. Rev. Lett. **126**, 087001 (2021).

[51] J. Zhang, Y.-S. Chen, D. Phelan, H. Zheng, M. R. Norman, and J. F. Mitchell, *Stacked Charge Stripes in the Quasi-2D Trilayer Nickelate* $La_4Ni_3O_8$, Proc. Natl. Acad. Sci. U.S.A. **113**, 8945 (2016).

[52] J. Zhang, A. Botana, J. Freeland, D. Phelan, H. Zheng, V. Pardo, M. Norman, and J. Mitchell, *Large Orbital Polarization in a Metallic Square-Planar Nickelate*, Nat. Phys. **13**, 864 (2017).

[53] J. Zhang, D. M. Pajerowski, A. S. Botana, H. Zheng, L. Harriger, J. Rodriguez-Rivera, J. P. C. Ruff, N. J. Schreiber, B. Wang, Y.-S. Chen, W. C. Chen, M. R. Norman, S. Rosenkranz, J. F. Mitchell, and D. Phelan, *Spin Stripe Order in a Square Planar Trilayer Nickelate*, Phys. Rev. Lett. **122**, 247201 (2019).

[54] O. O. Bernal, D. E. MacLaughlin, G. D. Morris, P.-C. Ho, L. Shu, C. Tan, J. Zhang, Z. Ding, K. Huang, and V. V. Poltavets, *Charge-Stripe Order, Antiferromagnetism, and Spin Dynamics in the Cuprate-Analog Nickelate* $La_4Ni_3O_8$, Phys. Rev. B **100**, 125142 (2019).

[55] M. Osada, B. Y. Wang, B. H. Goodge, S. P. Harvey, K. Lee, D. Li, L. F. Kourkoutis, and H. Y. Hwang, *Nickelate Superconductivity without Rare-Earth Magnetism:* $(La, Sr)NiO_2$, Adv. Mater. **33**, 2104083 (2021).

[56] S. W. Zeng, X. M. Yin, C. J. Li, C. S. Tang, K. Han, Z. Huang, Y. Cao, L. E. Chow, D. Y. Wan, Z. T. Zhang, Z. S. Lim, C. Z. Diao, P. Yang, A. T. S. Wee, S. J. Pennycook, and A. Ariando, *Observation of Perfect Diamagnetism and Interfacial Effect on the Electronic Structures in* $Nd_{0.8}Sr_{0.2}NiO_2$ *Superconducting Infinite Layers*, Nat. Commun. **13**, 743 (2022).

[57] L. Si, W. Xiao, J. Kaufmann, J. M. Tomczak, Y. Lu, Z. Zhong, and K. Held, *Topotactic Hydrogen in Nickelate Superconductors and Akin Infinite-Layer Oxides* ABO_2, Phys. Rev. Lett. **124**, 166402 (2020).

[58] O. I. Malyi, J. Varignon, and A. Zunger, *Bulk* $NdNiO_2$ *Is Thermodynamically Unstable with Respect to Decomposition while Hydrogenation Reduces the Instability and Transforms It from Metal to Insulator*, Phys. Rev. B **105**, 014106 (2022).

[59] H. LaBollita and A. S. Botana, *Electronic Structure and Magnetic Properties of Higher-Order Layered Nickelates:* $La_{n+1}Ni_nO_{2n+2} (n = 4–6)$, Phys. Rev. B **104**, 035148 (2021).

[60] C. T. Chen, F. Sette, Y. Ma, M. S. Hybertsen, E. B. Stechel, W. M. C. Foulkes, M. Schulter, S.-W. Cheong, A. S. Cooper, L. W. Rupp, B. Batlogg, Y. L. Soo, Z. H. Ming, A. Krol, and Y. H. Kao, *Electronic States in* $La_{2-x}Sr_xCuO_{4+\delta}$ *Probed by Soft-X-Ray Absorption*, Phys. Rev. Lett. **66**, 104 (1991).

[61] C. T. Chen, L. H. Tjeng, J. Kwo, H. L. Kao, P. Rudolf, F. Sette, and R. M. Fleming, *Out-of-Plane Orbital Characters of Intrinsic and Doped Holes in* $La_{2-x}Sr_xCuO_4$, Phys. Rev. Lett. **68**, 2543 (1992).

[62] A. Nag, M. Zhu, M. Bejas, J. Li, H. C. Robarts, H. Yamase, A. N. Petsch, D. Song, H. Eisaki, A. C. Walters, M. García-Fernández, A. Greco, S. M. Hayden, and K.-J. Zhou, *Detection of Acoustic Plasmons in Hole-Doped Lanthanum and Bismuth Cuprate Superconductors Using Resonant Inelastic X-Ray Scattering*, Phys. Rev. Lett. **125**, 257002 (2020).

[63] Y. Wang, G. Fabbris, M. Dean, and G. Kotliar, *EDRIXS: An Open Source Toolkit for Simulating Spectra of Resonant Inelastic X-Ray Scattering*, Comput. Phys. Commun. **243**, 151 (2019).

[64] EDRIXS website, https://github.com/NSLS-II/edrixs, accessed: 2021-09-27.

[65] See Supplemental Material at http://link.aps.org/supplemental/10.1103/PhysRevX.12.011055, which also includes Ref. [66] and details of the parameter dependence of the spectra.

[66] V. Bisogni, M. M. Sala, A. Bendounan, N. B. Brookes, G. Ghiringhelli, and L. Braicovich, *Bimagnon Studies in Cuprates with Resonant Inelastic X-Ray Scattering at the O K Edge. II. Doping Effect in* $La_{2-x}Sr_xCuO_4$, Phys. Rev. B **85**, 214528 (2012).

[67] K. Okada and A. Kotani, *Theory of Oxygen* 1*s Resonant X-Ray Emission in Edge-Share-Type Quasi-One-Dimensional Cuprates*, J. Phys. Soc. Jpn. **72**, 797 (2003).

[68] K. Okada and A. Kotani, *Copper-Related Information from the Oxygen* 1*s Resonant X-Ray Emission in Low-Dimensional Cuprates*, Phys. Rev. B **65**, 144530 (2002).

[69] K. Okada, *Effects of Hund's Coupling on Oxygen* 1*s X-Ray Absorption and Resonant X-Ray Emission in One-Dimensional Nickelates*, J. Phys. Soc. Jpn. **73**, 1681 (2004).

[70] C. Monney, V. Bisogni, K.-J. Zhou, R. Kraus, V. N. Strocov, G. Behr, J. Mlek, R. Kuzian, S.-L. Drechsler, S. Johnston, A. Revcolevschi, B. Bchner, H. M. Rnnow, J. van den Brink, J. Geck, and T. Schmitt, *Determining the Short-Range Spin Correlations in the Spin-Chain* Li_2CuO_2 *and* $CuGeO_3$ *Compounds Using Resonant Inelastic X-Ray Scattering*, Phys. Rev. Lett. **110**, 087403 (2013).

[71] C. Monney, V. Bisogni, K.-J. Zhou, R. Kraus, V. N. Strocov, G. Behr, S.-L. Drechsler, H. Rosner, S. Johnston, J. Geck, and T. Schmitt, *Probing Inter- and Intrachain Zhang-Rice Excitons in* Li_2CuO_2 *and Determining Their Binding Energy*, Phys. Rev. B **94**, 165118 (2016).

[72] S. Johnston, C. Monney, V. Bisogni, K.-J. Zhou, R. Kraus, G. Behr, V. N. Strocov, J. Mlek, S.-L. Drechsler, J. Geck, T. Schmitt, and J. van den Brink, *Electron-Lattice Interactions Strongly Renormalize the Charge-Transfer Energy in the Spin-Chain Cuprate* Li_2CuO_2, Nat. Commun. **7**, 10563 (2016).

[73] T. Plienbumrung, M. T. Schmid, M. Daghofer, and A. M. Ole, *Character of Doped Holes in* $Nd_{1-x}Sr_xNiO_2$, Condens. Matter **6**, 33 (2021).

[74] C. C. Chen, M. Sentef, Y. F. Kung, C. J. Jia, R. Thomale, B. Moritz, A. P. Kampf, and T. P. Devereaux, *Doping Evolution of the Oxygen K-Edge X-Ray Absorption Spectra of Cuprate Superconductors Using a Three-Orbital Hubbard Model*, Phys. Rev. B **87**, 165144 (2013).

[75] N. S. Headings, S. M. Hayden, R. Coldea, and T. G. Perring, *Anomalous High-Energy Spin Excitations in the High-T_c Superconductor-Parent Antiferromagnet* La_2CuO_4, Phys. Rev. Lett. **105**, 247001 (2010).

[76] H. T. Dang, A. J. Millis, and C. A. Marianetti, *Covalency and the Metal-Insulator Transition in Titanate and Vanadate Perovskites*, Phys. Rev. B **89**, 161113(R) (2014).

[77] K. Haule, *Exact Double Counting in Combining the Dynamical Mean Field Theory and the Density Functional Theory*, Phys. Rev. Lett. **115**, 196403 (2015).

[78] A. Hariki, M. Winder, and J. Kune, *Continuum Charge Excitations in High-Valence Transition-Metal Oxides Revealed by Resonant Inelastic X-Ray Scattering*, Phys. Rev. Lett. **121**, 126403 (2018).

[79] C. Weber, C. Yee, K. Haule, and G. Kotliar, *Scaling of the Transition Temperature of Hole-Doped Cuprate Superconductors with the Charge-Transfer Energy*, Europhys. Lett. **100**, 37001 (2012).

[80] Interestingly, this enhancement is not seen in a DFT Wannier analysis of the infinite-layer nickelate [16] and $La_4Ni_3O_8$ [81], where a value similar to the cuprates is found.

[81] E. M. Nica, J. Krishna, R. Yu, Q. Si, A. S. Botana, and O. Erten, *Theoretical Investigation of Superconductivity in Trilayer Square-Planar Nickelates*, Phys. Rev. B **102**, 020504(R) (2020).

[82] H. Eskes, L. H. Tjeng, and G. A. Sawatzky, *Cluster-Model Calculation of the Electronic Structure of CuO: A Model Material for the High-T_c Superconductors*, Phys. Rev. B **41**, 288 (1990).

[83] M. W. Haverkort, M. Zwierzycki, and O. K. Andersen, *Multiplet Ligand-Field Theory Using Wannier Orbitals*, Phys. Rev. B **85**, 165113 (2012).

[84] Y. Shen *et al.*, *Data Repository for: Role of Oxygen States in the Low Valence Nickelate* $La_4Ni_3O_8$, 10.5281/zenodo.5918536 (2022).

[85] I. Bozovic, *Atomic-Layer Engineering of Superconducting Oxides: Yesterday, Today, Tomorrow*, IEEE Trans. Appl. Supercond. **11**, 2686 (2001).

[86] M. Dean, R. Springell, C. Monney, K. Zhou, J. Pereiro, I. Božović, B. Dalla Piazza, H. Rønnow, E. Morenzoni, J. Van Den Brink *et al.*, *Spin Excitations in a Single* La_2CuO_4 *Layer*, Nat. Mater. **11**, 850 (2012).

[87] M. Dean, G. Dellea, R. Springell, F. Yakhou-Harris, K. Kummer, N. Brookes, X. Liu, Y. Sun, J. Strle, T. Schmitt *et al.*, *Persistence of Magnetic Excitations in* $La_{2-x}Sr_xCuO_4$ *from the Undoped Insulator to the Heavily Overdoped Non-superconducting Metal*, Nat. Mater. **12**, 1019 (2013).

[88] D. Meyers, H. Miao, A. C. Walters, V. Bisogni, R. S. Springell, M. d'Astuto, M. Dantz, J. Pelliciari, H. Y. Huang, J. Okamoto, D. J. Huang, J. P. Hill, X. He, I. Božović, T. Schmitt, and M. P. M. Dean, *Doping Dependence of the Magnetic Excitations in* $La_{2-x}Sr_xCuO_4$, Phys. Rev. B **95**, 075139 (2017).

[89] I. Bozovic and J. Eckstein, *Analysis of Growing Films of Complex Oxides by RHEED*, MRS Bull. **20**, 32 (1995).

[90] V. Y. Butko, G. Logvenov, N. Boovi, Z. Radovi, and I. Boovi, *Madelung Strain in Cuprate Superconductors—A Route to Enhancement of the Critical Temperature*, Adv. Mater. **21**, 3644 (2009).

[91] L. J. P. Ament, M. van Veenendaal, T. P. Devereaux, J. P. Hill, and J. van den Brink, *Resonant Inelastic X-Ray Scattering Studies of Elementary Excitations*, Rev. Mod. Phys. **83**, 705 (2011).

[92] H. Miao, J. Lorenzana, G. Seibold, Y. Y. Peng, A. Amorese, F. Yakhou-Harris, K. Kummer, N. B. Brookes, R. M. Konik, V. Thampy, G. D. Gu, G. Ghiringhelli, L. Braicovich, and M. P. M. Dean, *High-Temperature Charge Density Wave Correlations in* $La_{1.875}Ba_{0.125}CuO_4$ *without Spin–Charge Locking*, Proc. Natl. Acad. Sci. U.S.A. **114**, 12430 (2017).